

Excellence in Chemistry Research

**Announcing
our new
flagship journal**

- Gold Open Access
- Publishing charges waived
- Preprints welcome
- Edited by active scientists



Meet the Editors of *ChemistryEurope*



Luisa De Cola

Università degli Studi
di Milano Statale, Italy



Ive Hermans

University of
Wisconsin-Madison, USA



Ken Tanaka

Tokyo Institute of
Technology, Japan

DOI: 10.1002/cssc.201402670

Operando and In situ X-ray Spectroscopies of Degradation in $\text{La}_{0.6}\text{Sr}_{0.4}\text{Co}_{0.2}\text{Fe}_{0.8}\text{O}_{3-\delta}$ Thin Film Cathodes in Fuel Cells

Samson Y. Lai, Dong Ding, Mingfei Liu, Meilin Liu, and Faisal M. Alamgir*^[a]

Information from ex situ characterization can fall short in describing complex materials systems simultaneously exposed to multiple external stimuli. Operando X-ray absorption spectroscopy (XAS) was used to probe the local atomistic and electronic structure of specific elements in a $\text{La}_{0.6}\text{Sr}_{0.4}\text{Co}_{0.2}\text{Fe}_{0.8}\text{O}_{3-\delta}$ (LSCF) thin film cathode exposed to air contaminated with H_2O and CO_2 under operating conditions. While impedance spectroscopy showed that the polarization resistance of the LSCF cathode increased upon exposure to both contaminants at

750 °C, XAS near-edge and extended fine structure showed that the degree of oxidation for Fe and Co decreases with increasing temperature. Synchrotron-based X-ray photoelectron spectroscopy tracked the formation and removal of a carbonate species, a Co phase, and different oxygen moieties as functions of temperature and gas. The combined information provides insight into the fundamental mechanism by which H_2O and CO_2 cause degradation in the cathode of solid oxide fuel cells.

Introduction

Solid oxide fuel cells (SOFCs) have the potential to be one of the cleanest and most efficient chemical-to-electrical energy conversion systems.^[1] The excellent fuel flexibility allows direct conversion of hydrogen,^[2] coal gas,^[3] and transportation fuels^[4] to electricity. However, broad commercialization of SOFCs hinges on cost reduction. One of the barriers to commercialization is chemical stability and robustness of materials operating at high temperature. Contaminants in the gas phase can cause performance degradation and premature failure.^[5] Novel electrode materials and structures are needed to tolerate contaminants in the gas phase. Thus, rational design of new materials is vital to accelerating the process of discovery and implementation of SOFC technology.

One of the major difficulties in the rational design of novel cathode materials is the lack of fundamental understanding of electrode processes under operating conditions. The term *operando* is used to describe the experiments conducted under proper control of temperature, partial pressure of various gases, and electrical polarization to replicate or simulate the practical operating conditions. The information gained from an operando measurement can be used to better understand the mechanisms of chemical interactions on the surface, at interfaces, and in the bulk. Some prior operando experiments have been successful for low temperature polymer electrolyte fuel cells.^[6]

The high operating temperature of SOFCs presents a challenge in designing safe and effective experiments. Increased complexity also comes in the form of controlling experimental parameters while simultaneously accommodating the needs of the probing technique. Optical and infrared characterization methods have found success in operando experiments^[7] but synchrotron X-rays are highly desired for their wealth of element-specific information, such as chemical state, bond length, and coordination. Furthermore, the results of in situ experiments cannot necessarily be combined to predict the result of an operando experiment, similar to how ex situ results may fail to fully capture an in situ phenomenon. Operando spectroscopy is essential for providing insight into the reaction mechanisms and information for the rational design of novel materials.^[1a]

For SOFC materials, while many efforts have been focused on in situ X-ray absorption experiments, operando XAS studies that examine the material state under the combined stimulus of temperature, atmosphere, and electrical polarization have been budding in recent years. In some operando experiments on thin films of lanthanum-based perovskite cathodes, the response of the material surface to thermal annealing and electrical bias was examined through X-ray techniques but chemical interactions with contaminants in the gas were not explored.^[8] High temperature operando X-ray absorption studies can uniquely provide insight into the thermal and polarization effects on the oxidation states of specific elements, such as Ni in La_2NiO_4 .^[9] Operando XAS has also been essential in identifying complicated sulfur species at moderate temperatures resulting from a Ni/GDC anode being exposed to H_2S .^[10] For surface sensitive, gas interaction studies, the advent of ambient pressure X-ray photoelectron spectroscopy has led to many in situ and operando studies.^[11]

[a] S. Y. Lai, Dr. D. Ding, Dr. M. Liu, Prof. M. Liu, Prof. F. M. Alamgir

Center for Innovative Fuel Cell and Battery Technologies

School of Materials Science and Engineering

Georgia Institute of Technology

771 Ferst Drive NW, Atlanta, GA 30332-0245 (USA)

E-mail: faisal.alamgir@mse.gatech.edu

 Supporting Information for this article is available on the WWW under <http://dx.doi.org/10.1002/cssc.201402670>.

In this paper, we demonstrate the use of a custom-designed testing assembly for operando XAS studies of SOFC electrode materials under practical operating conditions. The operando cell may be configured for the study of cathode or anode materials and emphasizes surface information by using a glancing, incident X-ray angle, allowing key gas-solid interactions on or near electrode surfaces to be investigated under operating conditions. We studied the effects of CO_2 and H_2O gas contaminants on the electronic and local atomistic structure of the Fe and Co cations in a $\text{La}_{0.6}\text{Sr}_{0.4}\text{Fe}_{0.8}\text{Co}_{0.2}\text{O}_{3-\delta}$ (LSCF) thin film cathode of a symmetrical SOFC in operation. Together with complementary X-ray photoelectron spectroscopy (XPS) measurements, we are able to provide new insight into the poisoning mechanisms from H_2O and CO_2 under operating conditions.

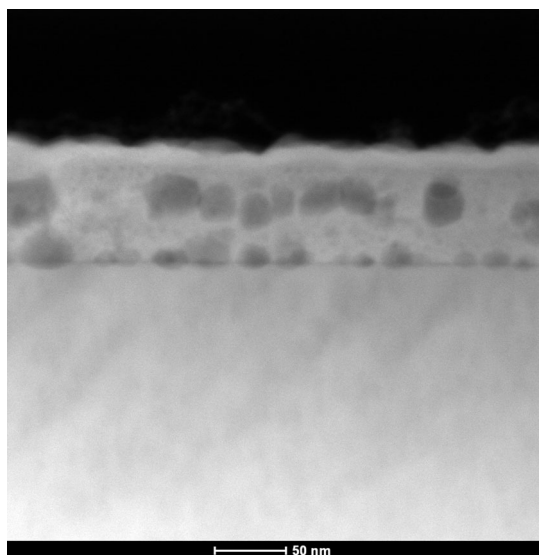


Figure 1. TEM image of the LSCF thin film cross-section.

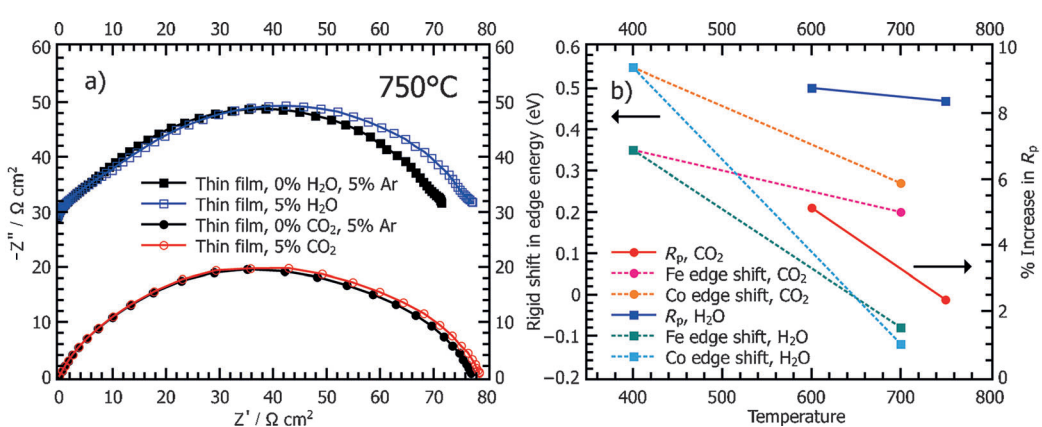


Figure 2. a) Impedance spectra of a thin film LSCF cathode show the increase in polarization resistance caused by H_2O and CO_2 . b) The correlation between performance, operating conditions, and rigid shifts in absorption edge energy can be observed.

Results and Discussion

Figure 1 shows a cross-sectional view of a thin-film LSCF cathode deposited on a single crystal YSZ substrate. The thickness of the LSCF film is about 70 nm and is clearly porous. The thin film allows the X-ray to probe the triple phase boundaries at the cathode/electrolyte interface while the porosity creates high specific surface area of LSCF so that there are more atoms active in the solid/vapor interface region.

Figure 2a shows some typical impedance spectra of the test cells with thin-film LSCF in the presence of 5% Ar, 5% CO_2 , and 5% H_2O at 750 °C. The use of 5% Ar is to eliminate the Nernst effect or the contribution from a difference in oxygen partial pressure due to the dilution of oxygen when air is mixed with other contaminant gases (CO_2 and H_2O). The increase in the polarization resistance is 2.4% and 8.4% for CO_2 and H_2O , respectively, meaning that both cause degradation in the performance at operating temperatures. Corresponding impedance spectra at 600 °C are shown in Figure S1 in the Supporting Information. Figure 2b shows the correlation between the rigid shift in the XAS edge energy and the percentage change in polarization resistance as a function of temperature and gas contaminant. An increase in the binding energy of electrons in core-hole spectroscopy (XAS, XPS) is related to a net electron transfer away from the absorbing atom, which chemically corresponds to oxidation. At lower temperatures, both Fe and Co cations tend to become oxidized and the polarization resistance tends to increase. With increasing temperature, the positive shift in the edge energy (indicating oxidation) decreases with H_2O , showing a stronger temperature dependence than CO_2 . While exposure to H_2O results in an overall higher polarization resistance, the relative change in polarization resistance due to temperature is larger for exposure to CO_2 . The trend may be caused by a saturation effect of H_2O on the surface, which could be corroborated by the shift in edge energy. In contrast, the shift in edge energy from exposure to CO_2 is less significant but the polarization resistance is more influenced by temperature. This phenomenon is the first indicator that while both H_2O and CO_2 cause performance degra-

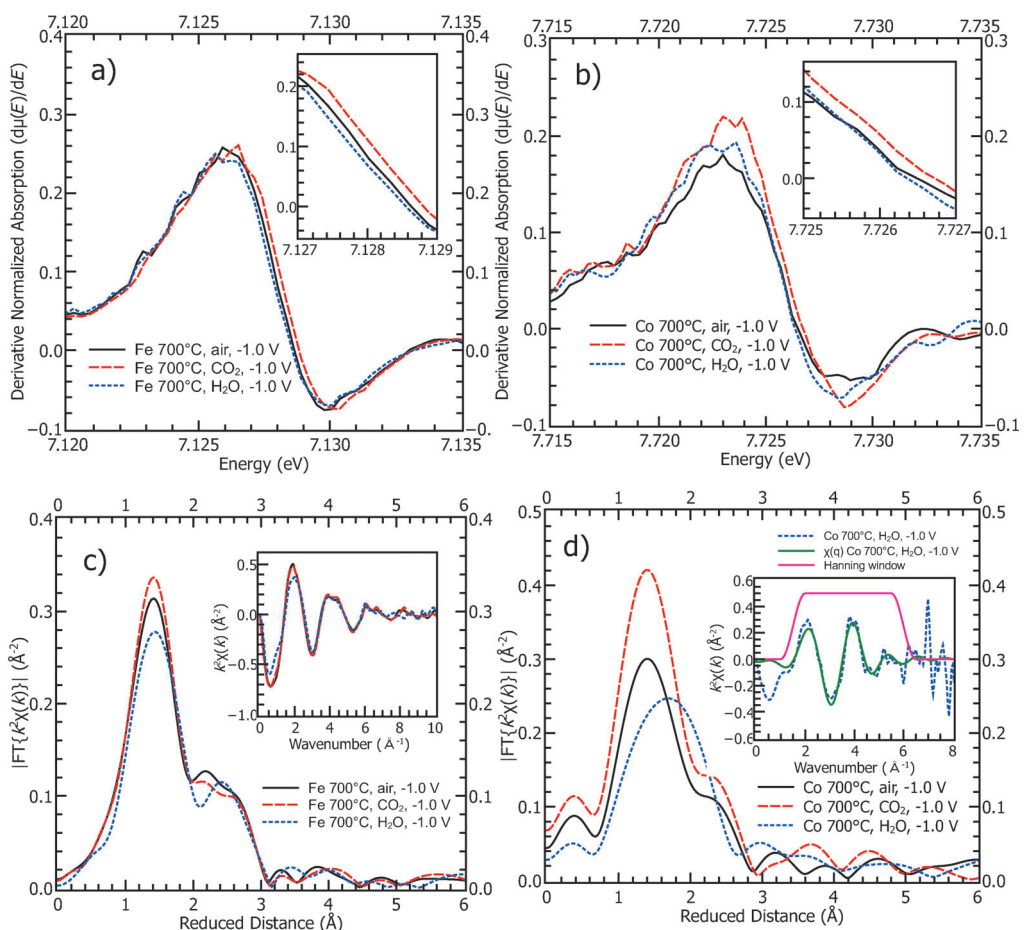


Figure 3. The derivative of the near-edge absorption of a) Fe and b) Co at 700 °C under cathodic bias while exposed to H₂O and CO₂. Closer views of the edge shift are provided in the insets. The EXAFS data for c) Fe and d) Co support the observation of oxidation. The inset in c) shows the wavevector form of the absorption spectroscopy. The inset in d) compares the wavevector form of the spectrum under H₂O exposure to the backwards Fourier transform X(q) and indicates the window used for the forward Fourier transform. A k^2 factor was used to weight the relative variation in the absorption coefficient, $\chi(k)$, before the Fourier transform.

tion, the nature of the interactions with the LSCF cathode is distinctly different, as will be discussed later.

Operando XAS was performed to better understand the chemical influences of temperature and gas contaminants like CO₂ and H₂O under operating conditions. Figure 3 shows the derivative of the normalized absorption for Fe and Co, which more clearly depicts the rigid shifts in edge energy in the near-edge (XANES) region. Examples of the full XAS spectrum in energy space are included in the Supporting Information. When the cathode is cathodically polarized, the presence of CO₂ causes a slight oxidation of Fe and Co while that of H₂O has a slightly reducing or no effect on the oxidation state. The edge energy shifts in Fe and Co under CO₂ are 0.20 and 0.27 eV, respectively, referenced to their polarized state under air without contaminants. The oxidizing effects of CO₂ are supported by the Fourier-transformed extended X-ray absorption fine structure (FT-EXAFS) of Fe and Co, in which a significant increase in the magnitude of the first-shell coordination peak represents an increase in the number of oxygen bonds relative to the cathode in air. Conversely, the magnitude of the first-shell coordination peak decreases when H₂O is introduced.

Additionally, H₂O has little influence on the overall local structure of the Fe but significantly affects the Co local structure. The new peak is lower in magnitude and has a broader full width half maximum (FWHM) than the first-shell coordination peak, which is likely due to the convolution of two smaller peaks, and the phase-shift uncorrected length is 0.31 Å longer. It is speculated that the local structure distortion is caused by elongated Co bonds, which could be to a hydroxide or carbonate ligand based on the gas contaminant introduced. Further insight into the chemical phenomena is provided by synchrotron-based XPS, as discussed later.

At 400 °C, the degree of oxidation is increased in both Fe and Co, as shown in Figure 4, which correlates with the larger degradation in performance at lower temperatures. The edge energy shift is approximately the same whether the cathode is exposed to CO₂ or H₂O and is 0.35 and 0.55 eV for Fe and Co, respectively. As previously exhibited by the FT-EXAFS at 700 °C, an oxidation shift in the edge energy is accompanied by an increase in the magnitude of the first-shell coordination peak, representing the increase in the number of oxygen ligands caused by exposure to CO₂ and H₂O. Beyond the first-shell co-

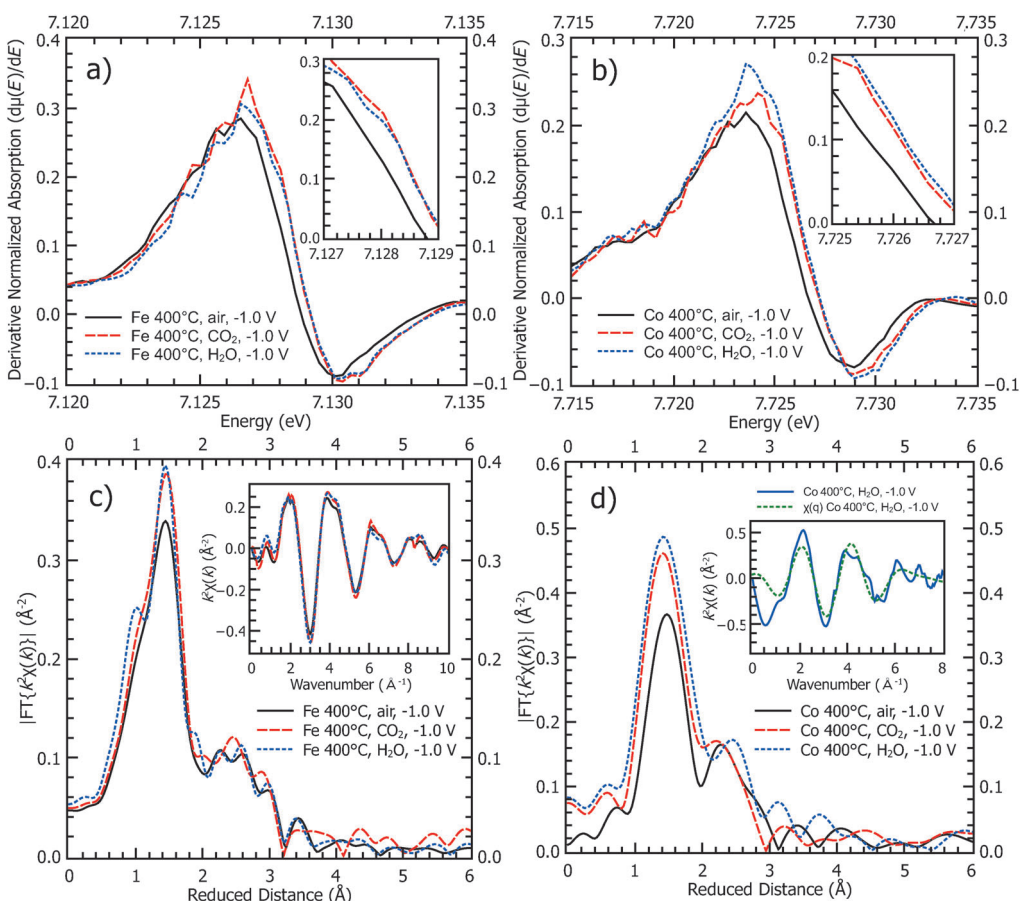


Figure 4. The derivative of the near-edge absorption of a) Fe and b) Co at 400 °C under cathodic bias while exposed to H₂O and CO₂. Closer views of the edge shift are provided in the insets. The EXAFS data for c) Fe and d) Co support the observation of oxidation. The inset in c) shows the wavevector form of the absorption spectroscopy while the inset in d) compares the wavevector form of the spectrum under H₂O exposure and the backwards Fourier transform X(q). A k^2 factor was used to weight the relative variation in the absorption coefficient, $\chi(k)$, before the Fourier transform.

ordination, the overall Fe local structure is relatively stable. The Co local structure also exhibits similar evidence of oxidation, based on the increase in magnitude of the first-shell coordination peak and a relatively stable structure with none of the deformations observed at 700 °C.

Synchrotron-based XPS was performed to complement the operando XAS results with a highly surface sensitive technique that could better identify new ligand formation, particularly carbonates. The C 1s photoemission spectra shown in Figure 5 belong to the as-prepared LSCF thin film at 25, 750, and 25 °C after cooling in an equal mixture of H₂O and CO₂. The reference condition indicates that the spectrum was collected under ultrahigh vacuum (UHV) conditions without an immediately prior exposure to CO₂ and H₂O. The adventitious carbon peak at 284.8 eV was used for calibrating the binding energy scale. At a higher binding energy of 288.4 eV, a small shoulder can be identified as related to C 1s emission from a carbonate-type of species. As this species is present on the sample prior to the thermal and exposure treatments that follow, this feature is ascribed to adventitious carbonate on the surface. The binding energy of the shoulder peak closely matches literature values for various carbonate species.^[12] The shoulder peak is clearly absent in the spectrum collected at 750 °C. It is

presumed that the carbonate species that previously existed decomposed into CO₂ and the respective oxide. After cooling in the presence of H₂O and CO₂, the carbonate peak reappears.

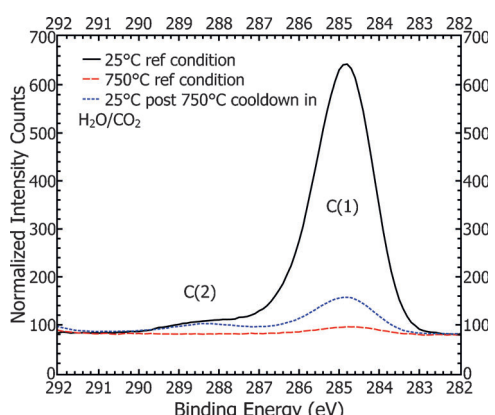


Figure 5. XPS results which indicate that carbonate formation disappears at high temperature and then reappears on cooling in the presence of CO₂ and H₂O. The reference condition indicates measurement of spectra under UHV conditions without an immediately prior exposure to CO₂ and H₂O.

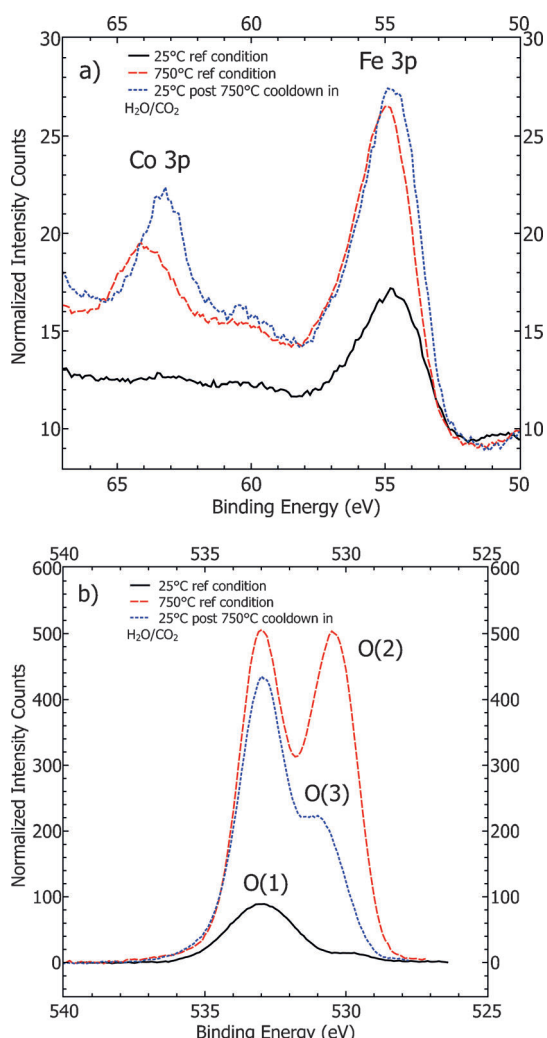


Figure 6. a) Fe and Co 3p and b) O 1 s photoemissions from XPS. O(1), O(2), and O(3) identify photoemission peaks characteristic of surface oxygen, lattice oxygen, and hydroxide oxygen species, respectively.

implying that the carbonate species reformed on the surface during the thermal quenching of the LSCF thin film.

In Figure 6, the Fe and Co 3p photoemissions are shown. The Fe photoemission is relatively stable, showing slight oxidation at high temperature and slight reduction upon cool down under H_2O and CO_2 . In contrast, no Co 3p photoemission is detectable at room temperature, which is typically in the range of 59 to 61 eV for the 2+ and 3+ oxidation states.^[13] Upon heating, a new peak at 64 eV is formed, which is believed to be Co-related but there is little literature to identify a formal peak at such a high energy. The current assumption is that the Co species is a Co^{3+} species with highly electronegative ligands. After cooling down under H_2O and CO_2 , the new photoemission peak remains, suggesting that the Co-containing phase was irreversibly formed, and shifts to lower binding energy. This new Co-containing phase is presumed to be an oxide resulting from the decomposition of the carbonate. The bonding of hydroxide ions to the oxide during the cool down, as evidenced below by the O 1s photoemission, would cause

a net reduction in the Co oxidation state and thus, a shift in the 3p photoemission to lower binding energy.

Also shown in Figure 6 is the O 1s photoemission. At room temperature, the main peak labeled O(1) is attributed to surface oxygen, although other possibilities have been suggested,^[14] while the lesser peak labeled O(2) at 529.6 eV can be matched to lattice oxygen.^[14a, 15] Since the peak at high binding energy increases, rather than diminishes, at 750 °C, the temperature at which the carbonate signal was depleted, it is concluded that the O(1) peak is not solely representative of oxygen in carbonate but the signal is likely convoluted. Upon heating, adventitious carbon is removed, which increases overall signal intensities, and the carbonate decomposes into an oxide, which populates the surface with oxygen in a lattice valence state. The cool down under H_2O and CO_2 causes significant hydroxide and carbonate formation, the former resulting in the peak shoulder photoemission, labeled O(3), which is characteristic of oxygen in a hydroxide,^[13a, 16] and the latter contributing to the greater intensity of the O(1) peak relative to the initial reference condition.

To separate and identify the individual contributions of different operating parameters, *in situ* XAS was performed under varying conditions. In Figure S2, Supporting Information, the presence of CO_2 causes a slight edge energy shift of 0.07 eV in Fe at 700 °C. When the same experiment was performed with cathodic bias, the edge energy shift in Fe was 0.20 eV. In the case of Co, the presence of CO_2 caused an edge energy shift of 0.21 eV at 700 °C. The same experiment with cathodic bias caused an edge energy shift of 0.27 eV. Again, the influence of cathodic bias led to a larger magnitude shift in the edge energy. In Figure S3, Supporting Information, it can be seen that, as with the operando results, the oxidizing effect of CO_2 is greater at 400 °C than at 700 °C. The edge energy shifts are 0.29 and 0.34 eV for the Fe and Co edges, respectively, compared to 0.35 and 0.55 eV edge shifts as measured in operando at 400 °C. As with the trend at 700 °C, the operando results at 400 °C indicate a greater magnitude in edge energy shift, which implies that the cathodic bias caused more severe oxidation.

The influence of cathodic bias was examined *in situ*. Shown in Figure S4, Supporting Information, is the derivative of the Fe XANES spectrum after normalization, with and without polarization at 400 °C. The application of a cathodic bias caused an edge energy shift of -0.11 eV, which is expected as a cathodic bias would have a slight reducing effect. A similar effect was observed in the Co XANES spectrum under the same conditions, as seen in Figure S5, Supporting Information.

Figure 7 summarizes how the edge shifts in energy caused by exposure to CO_2 were greater for both Fe and Co under operando conditions than they were under *in situ* conditions without polarization at both 400 and 700 °C. The presence of CO_2 has an oxidizing effect and cathodic bias exacerbates the degree of oxidation as measured by the shift in the absorption edge energy.

The combined results of the operando XAS and the synchrotron XPS provide some useful insights into the chemical phenomena, particularly on the differences in the influence of H_2O

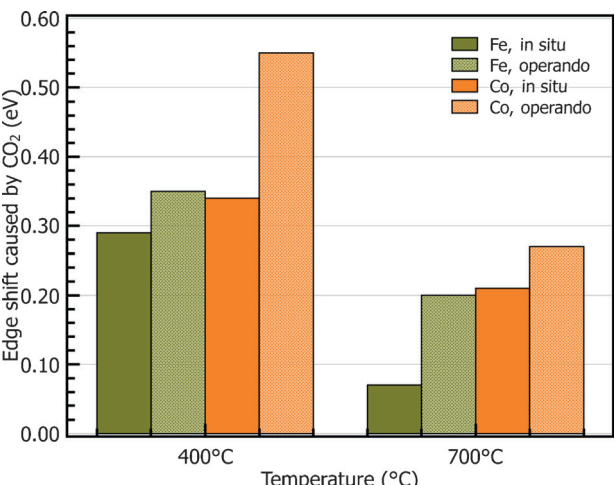


Figure 7. Absorption edge shift in energy in both Fe and Co caused by the presence of CO_2 at 400 °C and 700 °C. The shift is greater in operando experiments than in in situ experiments.

and CO_2 . Based on the synchrotron-based XPS results, it is speculated that the carbonate species forms with Co at room temperature, according to Equation (1). At high temperature, the carbonate species decomposes into Co_3O_4 and releases CO_2 per Eq. (2). Subsequent exposure to CO_2 results in slight oxidation of Fe and Co. Thus, the adsorption of CO_2 was consuming oxygen vacancies on the surface and slightly increasing the polarization resistance. Continuous formation and decomposition of CoCO_3 from high temperature exposure to CO_2 would contribute to long-term degradation. The proposed reaction mechanisms are depicted schematically using Kröger–Vink notation, where superscript 'X' indicates a neutral charge relative to the nominal charge in a stoichiometric lattice, in Figure 8, and in Equations (1) and (2).

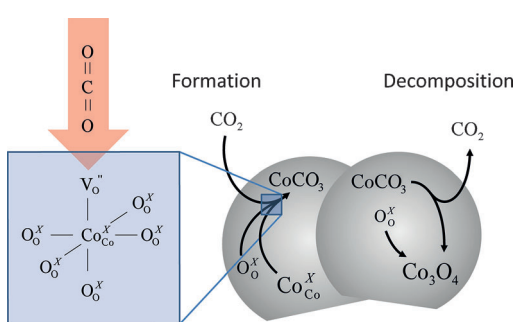
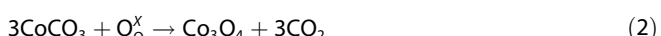


Figure 8. Reaction mechanisms proposed for the formation and decomposition of cobalt carbonate, using Kröger–Vink notation. The CO_2 is hypothesized to bond to the Co atom in the octahedral site through an oxygen vacancy.



The role of H_2O also has a significant effect on both the oxidation states and local structure. Given that the exposure to H_2O appeared to cause oxidation in Fe and Co at 400 °C, it would be expected that the same effect, but to a lesser degree would occur at 700 °C, similar to what was observed from CO_2 . The increase in polarization resistance during H_2O exposure observed in the impedance measurements also supports this expectation. However, the effect of H_2O on the oxidation of Fe and Co at 700 °C was slightly reducing or negligible, respectively. One plausible explanation is that if hydroxide anions were to replace oxygen anions in the perovskite lattice, the net result could be that the Fe and Co cations experience a slight reduction. As hydroxide anions diffuse into the bulk, they would also impede the diffusion pathways for oxygen vacancies, resulting in the observed increased polarization resistance. Disruption of the diffusion pathways for oxygen vacancies below the surface could explain why the magnitude of the increase in polarization resistance is greater under H_2O relative to CO_2 .

Water vapor was also observed to have a significant effect on the Co local structure but less so on the Fe structure. If the deformation in local structure in Co is attributed to the formation of Co_3O_4 , then the presence of water may likely assist in that reaction. For example, a hydroxide anion may provide a source of oxygen anions to form carbonate ligands. Since the X-ray beam is probing to some extent into the bulk, a combination of both nominal Co in the LSCF structure and Co in the segregated oxide phase would contribute to the broad FT-EXAFS peak. The presence of a segregated Co oxide is also supported by the Co 3p and O 1s photoemissions in XPS. The indication that a Co oxide is forming could explain the gradual but continuous long-term degradation behavior. On the other hand, Fe cation FT-EXAFS does not indicate significant change in the local structure when exposed to H_2O and its photoemission shows relatively little change during high temperature or after reaction with H_2O and CO_2 . It should be noted that loss of B-site cations due to phase segregation could lead to A-site cation stoichiometric imbalance, resulting indirectly in the widely observed Sr segregation.^[11c,17] The susceptibility of Co to diffusion and phase segregation, as suggested by both FT-EXAFS and XPS, should be explored in future experiments.

The operando results at 400 °C show that both H_2O and CO_2 exhibit strong oxidation effects on Fe and Co. Both the Fe and Co local structures indicate an increase in the magnitude of the first coordination shell peak, suggesting that the oxygen vacancies are depleted, which explains the increase in the polarization resistance observed in impedance spectroscopy. However, the Fe and Co FT-EXAFS results did not show a significant difference between the CO_2 and H_2O . The reason these effects differ from those observed at high temperature may also be because the carbonate species present at room temperature, as detected by XPS, may be stable on the surface at 400 °C and prevent H_2O from interacting with the Fe and Co and diffusing further. It may be that high temperatures, at which the carbonate decomposes, are required for the H_2O to have an influence.

One of the key aspects of this study was to demonstrate the unique capabilities and advantages of operando experiments. The in situ experiments indicate that the cathodic bias has a reducing effect and the CO₂ had an oxidizing effect on both Fe and Co. However, in the operando experiment, the presence of cathodic bias increased the degree of oxidation caused by CO₂. Therefore, the combined effects cannot be predicted by a linear sum. The effect of cathodic bias may be attributed to generating partially reduced oxygen species that can react with CO₂ on the surface to form carbonates ligands. If these surface carbonates bond to the transition metal cations via an oxygen atom occupying an oxygen vacancy, then the overall oxidation state of the transition metal cations would increase. This effect may be less apparent at high temperatures because the carbonate would be decomposing and the remaining oxygen atom could diffuse to the substrate. At lower temperatures, an accumulation of stable carbonate surface species could lead to a greater average oxidation state of Fe and Co. Without the cathodic bias to catalyze the oxygen reduction reaction, fewer carbonate species on the surface would then lead to less oxidation of Fe and Co and thus explain the smaller shifts in edge energy observed in the in situ experiments. These phenomena emphasize the uniqueness and necessity of operando experiments to obtain better insights into the fundamental mechanisms at work.

Conclusion

We have designed and implemented an operando SOFC testing assembly capable of probing the electronic and local atomistic structure of a specific element in an operating cathode of a quasi-symmetrical cell with proper control of temperature, gas contamination, and electrical polarization. These operando experiments provided useful insight into the different influences of CO₂ and H₂O on the Fe and Co cations of the LSCF thin film cathode. It was found that the magnitude of the increase in polarization resistance is correlated with the degree of oxidation according to the shift in edge energy for both Fe and Co, but the influence of temperature on the polarization resistance differed between H₂O and CO₂. The XANES indicated that CO₂ had slightly oxidizing effects while H₂O had a neutral effect on Co and slightly reducing effect on Fe at 700 °C. However, the FT-EXAFS showed that Co local structure underwent significant deformation in the first coordination shell, resulting in an elongated bond length. Meanwhile, the Fe local structure appeared to be relatively stable and only increased in the magnitude of the first coordination shell peak, indicating filling of oxygen vacancies by lattice oxygen, carbonate, or hydroxide ligands. Synchrotron-based XPS complemented the operando XAS by providing information about the stability of the carbonate species at 400 °C and its instability at 750 °C. The combination of these techniques, along with impedance spectroscopy and in situ XAS, enabled us to speculate that the Co cation is particularly susceptible deformation in the local structure and phase segregation over time, and thus, it should be the focus of future investigations and rational materials design. Lastly, a comparison of the results from operando and in situ

testing revealed that operando results cannot be predicted by their in situ components, strengthening the rationale for pursuing challenging operando experiments.

It is presumed that H₂O may play a key role in the transformation of CO₂ to CO₃²⁻ readily. However, further investigations using high pressure synchrotron-based XPS are warranted to fully elucidate the details of CO₂ and H₂O interactions under operando techniques. Operando experiments, such as those described above, will also be of further use in understanding how solution-infiltrated coatings for SOFC electrode materials confer their beneficial properties.

Experimental Section

Material synthesis method for electrochemical impedance spectroscopy: To test the LSCF thin film cell performance through electrochemical impedance spectroscopy (EIS), we fabricated quasi-symmetrical cells composed of a porous LSCF electrode that serves as the counter electrode, a dense thin film LSCF electrode that serves as the working electrode, and a thick electrolyte of gadolinium-doped ceria (GDC). Dense GDC pellets were achieved by dry-pressing the GDC powders (Daiichi, Japan) at 300 MPa and sintering at 1450 °C for 5 h. A polishing process was applied for the one side of the GDC pellet and LSCF ink was screen-printed on the other side with a firing process of 1080 °C for 2 h. A dense LSCF thin film was sputtered on the polished side and annealed at 800 °C for 1 h. Since the counter electrode is highly porous, its contribution to the overall polarization resistance is much smaller than that of the thin film LSCF electrode. This is an effect resulting from the lower concentration polarization of a porous microstructure, whereas a thin film would be diffusion-limited. This has been demonstrated in our previous work.^[18] As a result, when the overall polarization resistance is measured and the thin film is influenced by exposure to air containing H₂O or CO₂, the change in the overall polarization resistance can be mostly attributed to the thin film. Thus, the electrochemical performance of the quasi-symmetrical cell is dominated by the thin film LSCF working electrode. Impedance spectra were acquired using a Solartron 1255 HF frequency response analyzer interfaced with an EG&G PAR potentiostat model 273 A with an amplitude of 10 mV in the frequency range from 0.1 Hz to 100 kHz. Compressed air was used as the carrier gas and was mixed with the desired gas at a specific flow rate to obtain desired concentration as a volumetric percentage. To obtain 5% Ar or CO₂, for example, the flow rate of air set to 95 sccm and Ar or CO₂ as 5 sccm, respectively. To achieve a concentration of 5% H₂O, a humidifier was used to maintain the temperature of the water at 33 °C, which corresponds to a 5.04 kPa of saturated vapor pressure of water, thus 4.98% as volumetric percentage.

To prepare an ideal cell for X-ray characterization, we began with a single crystal of YSZ (1 cm x 1 cm x 0.1 cm). A quasi-symmetrical cathode cell configuration was again used, with a porous LSCF counter electrode with a Sm_{0.2}Ce_{0.8}O_{1.95} (SDC) buffer layer and an LSCF thin film working electrode, which would be open to gas contaminants and X-rays for characterization. The porous LSCF counter electrode with a thickness of 50 µm was fabricated via tape-casting using a commercial powder from Fuel Cell Materials, as described previously.^[5,19] A 5 mm circular electrode was created by a hole puncher and was laid on top of an SDC layer, which was drop-coated as a slurry on the unpolished side of the YSZ single crystal. The assembly was co-fired at 1080 °C for 2 h before LSCF thin film cathode was sputter deposited on the polished side.

For the LSCF thin film cathode, we desired a cathode with a model geometry so that the interaction phenomenon would be limited to a controlled region of study. Thus, we attempted to fabricate a 200 nm LSCF thin film on YSZ single crystal by two stages of sputtering 100 nm. The cell was annealed at 500 °C for 1 h in air in between the sputtering stages to relieve mechanical stress and reconstruct the surface before the second stage of sputtering. A final annealing stage at 800 °C for 1 h in air was used to complete the synthesis. Electrical contacts were made using silver wire attached via silver paste. A FEI Tecnai F30 Super Twin field emission gun transmission electron microscope (TEM) with a 300 KV accelerating voltage was used to acquire the scanning transmission electron microscopy (STEM) and TEM images.

Testing assembly design: A custom furnace was designed and constructed in-house to satisfy all of the requirements for an operando experiment. A schematic of the furnace design is shown in Figure 9. The external housing was made using a 1.5 mm thick alu-

A WaveNano potentiostat (Pine Instruments) was used to apply the electrical bias. Since no reference electrode was included in the design, the counter electrode was used as the reference electrode. A key challenge of the experiment was obtaining a good fluorescent yield and signal-to-noise ratio. Traditionally, maximizing the detector's solid angle for photon capture is achieved by bringing the detector close to the sample. However, difficulties originate from the large amount of infrared light coming from the furnace and the convective heat transfer to the detector in close proximity. As a compromise, increased distance to detector and an IR filter are recommended for optimal signal quality. For detectors used in close proximity, active cooling with flowing water or another fluid is recommended both to improve signal quality and safeguard the detector's heat-sensitive components.

Another key challenge was calibration of the beam spot size to maximize incidence on the sample while using the glancing angle geometry to emphasize data collection from the surface. The sample angle must be steep enough to be reliably covered by the beam spot size but shallow enough to splay the beam across the maximum amount of area. Additionally, a sufficient amount of the beam must pass over the sample into the downstream ion chambers for measurement of the reference foil's absorption. A shallow angle of 2° will splay a beam with a 1.0 mm vertical height across 28.7 mm of angled length, which is sufficient to cover a 10 mm long sample (that only blocks 0.35 mm of the vertical beam height at a 2° angle) and extends over the sample into the downstream reference ion chambers. With respect to the information depth, the absorption length of the LSCF using 7,112 eV (Fe K-edge) photons is 7.2 μm, which at a 2°C incident angle, results in an incident photon penetration depth of about 250 nm normal to the surface. Although photons can penetrate beyond one absorption length, due to the exponential decay of Beer's Law, the majority of the signal originates from within the first absorption length.

To achieve the aforementioned considerations experimentally, a large piece of fluorescent paper was used to optimize the initial beam spot size. After the *in situ* testing assembly was in place, a thin square of fluorescent paper was laid over the sample and used to further optimize the beam size, sample height, and angle. After removing the fluorescent paper, the sample height was then adjusted to correct for the thickness of the fluorescent paper.

Operando experimental conditions: The temperature recorded is based on a K-type thermocouple placed inside of the furnace. The gas contaminant was introduced via a glass pipet inserted through a small hole in the Kapton X-ray window and positioned toward the cell but not in the path of the X-ray beam. To introduce water vapor, nitrogen as a carrier gas was bubbled through a heated flask of water between 55 and 60 °C. The electrical polarization is the voltage across the whole cell as applied by the potentiostat. The combinations of testing parameters are shown in the Table 1.

X-ray absorption spectroscopy: XAS was performed at Beamline X18B of the National Synchrotron Light Source (NSLS) at Brookhaven National Laboratory (BNL). Incident photon energy was calibrated using an Fe foil and set at 7112.0 eV. The beamline uses a channel cut Si(111) double monochromator system with vertical and horizontal slits to control the beam spot size to be 8 mm wide and 1 mm in height. Higher harmonics are suppressed by detuning the second monochromator crystal to allow 70% of the maximum intensity using a piezoelectric picomotor. Ionization chambers filled with the appropriate mixture of nitrogen and argon gas were used to measure the incident, transmitted, and reference X-ray intensi-

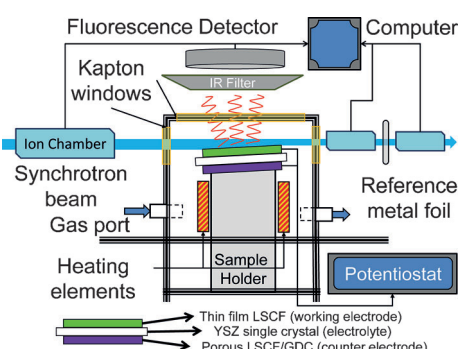


Figure 9. Schematic of the operando XAS testing assembly, which controls the temperature, atmosphere, and polarization while allowing a glancing incidence X-ray beam to interact with a sample and a reference foil through Kapton film windows.

minum sheet for the furnace walls and a 3.18 mm thick aluminum sheet (both McMaster) as a support base with flanges for safe handling while the furnace was hot. Heating elements consisted of two Watlow E2J80L12H 6.35 mm diameter cartridge heaters. The cell was affixed to a 9.5 mm diameter (7.0 mm inner diameter) Type 321 high strength stainless steel tube (McMaster) using a silver-based electrically conductive adhesive (Shanghai Research Institute for Synthetic Resins). The use of a stainless steel tube aids in heat conduction to the cell, which is exposed for spectroscopy purposes. For the current collection of the top side of the cell, 0.5 mm diameter silver wire was threaded through a two-bore 3.18 mm diameter alumina tube (Ortech, Inc.) and twisted together at the end for mechanical strength. The bores in the alumina tube helped prevent electrical shorting and the tube itself was tied to the sample holder tube using silver wires. Alumina fish spine beads were threaded on the protruding silver wire to electrically isolate a sufficient length to reach the alligator clips used by the potentiostat. The cartridge heaters, fuel cell sample holder, and the alumina tube were held in place by a pair of insulation bricks through individually machined holes. Externally, the sample holder was clamped to a crossbeam support between the support base flanges. The insulation was also hollowed out to create an air gap between the sample holder and the cartridge heaters for heat conduction. The maximum reliable temperature the cartridge heaters could reach is 700 °C. The X-ray window material used was Kapton film.

Table 1. Experimental conditions during the operando experiment. Flow of gas contaminant was 30 mL min^{-1} when not using ambient air.

Classification	Temperature [°C]	Electrical polarization	Gas contaminants
in situ	400	open circuit	air, CO_2
in situ	700	open circuit	air, CO_2
operando	400	applied, -1.0 V	air, CO_2 , 18–20% H_2O in N_2
operando	700	applied, -1.0 V	air, CO_2 , 18–20% H_2O in N_2

ties. A passivated implanted planar silicon (PIPS) detector was employed overhead to capture the fluorescent X-ray signal.

X-ray photoelectron spectroscopy: Synchrotron-based soft XPS was performed at Beamline U12A of the NSLS at BNL using a photon energy of 600 eV for high surface specificity. The same kind of LSCF thin film symmetrical cathode sample was mounted on a tungsten wire heating stage attached to the manipulator arm. Reference photoelectron spectra were collected at 25 °C and 750 °C under UHV without any in situ gas exposure. Afterward, the sample was cooled to 25 °C in an equal mixture of H_2O and CO_2 at a roughly constant partial pressure. After evacuating the chamber to UHV conditions, the photoemission spectra were collected again.

Data analysis: Data processing for the X-ray absorption data was performed using the Athena program in the Demeter software package.^[19] Multiple scans were deglitched by hand, aligned using derivatives of the accompanying reference foil scan, merged using raw absorption $\mu(E)$, and normalized by hand-picked pre-edge and post-edge ranges, which were optimized for maximum range and linearity. Smoothing was conducted with three-point averaging for eleven repetitions. The energy scale was calibrated using the data from a Fe reference foil. Some R_{bkg} values were adjusted slightly but typically a value of 1.0 was sufficient. Edge shifts in energy were measured according to the difference in the derivative curves at the abscissa. A Hanning window was used for the forward Fourier transform and chosen in the k-space region where the signal-to-noise ratio was acceptable. Since data were compared across the same temperatures, the same k-range was used for each set of data. Radial distances in the Fourier-transformed data were not corrected for phase shift.

For the XPS data, the binding energy scale was calibrated by setting the adventitious carbon peak to 284.8 eV. For normalization of the intensity, raw intensity counts were divided by the product of the number of scans, the dwell time for energy step (constant for all scans), and the mesh current, which accounts for the gradual decay in the intensity of the incident synchrotron beam. The normalized data were then imported into XPSPeak v4.1 for background subtraction using a Shirley background.

Acknowledgements

This work was supported as part of the HeteroFoAM Center, an Energy Frontier Research Center funded by the U.S. Department of Energy, Office of Science, Office of Basic Energy Sciences, under Award Number DE-SC0001061. The authors would like to acknowledge the technical expertise provided by Nebosja Marinkovic at beamline X18B and Peter Albrecht at U12A at the NSLS. The authors also appreciate the technical advice and discussions with

Dr. Yangping Li and Xiaxi Li. Use of the National Synchrotron Light Source, Brookhaven National Laboratory, was supported by the U.S. Department of Energy, Office of Science, Office of Basic Energy Sciences, under Contract No. DE-AC02-98CH10886. Samson Y. Lai would like to thank the National Science Foundation Nanostructured Materials for Energy Storage

and Conversion (NESAC) IGERT program for traineeship support under Award Number 1069138. The authors declare no competing financial interest.

Keywords: ceramics • EXAFS spectroscopy • fuel cells • photoelectron spectroscopy • X-ray absorption spectroscopy

- [1] a) M. Liu, M. E. Lynch, K. Blinn, F. M. Alamgir, Y. Choi, *Materials Today* **2011**, *14*, 534–546; b) N. Q. Minh, *Solid State Ionics* **2004**, *174*, 271–277.
- [2] L. Yang, S. Wang, K. Blinn, M. Liu, Z. Liu, Z. Cheng, M. Liu, *Science* **2009**, *326*, 126–129.
- [3] L. Yang, Y. Choi, W. Qin, H. Chen, K. Blinn, M. Liu, P. Liu, J. Bai, T. A. Tyson, M. Liu, *Nat. Commun.* **2011**, *2*, 1–9.
- [4] M. Liu, D. Ding, K. Blinn, X. Li, L. Nie, M. Liu, *Int. J. Hydrogen Energy* **2012**, *37*, 8613–8620.
- [5] S. J. Benson, D. Waller, J. A. Kilner, *J. Electrochem. Soc.* **1999**, *146*, 1305–1309.
- [6] a) E. Principi, A. Di Cicco, A. Witkowska, R. Marassi, *J. Synchrotron Radiat.* **2007**, *14*, 276–281; b) A. E. Russell, S. Maniguet, R. J. Mathew, J. Yao, M. A. Roberts, D. Thompsett, *J. Power Sources* **2001**, *96*, 226–232; c) E. A. Lewis, I. Kendrick, Q. Jia, C. Grice, C. U. Segre, E. S. Smotkin, *Electrochim. Acta* **2011**, *56*, 8827–8832.
- [7] a) J. D. Kirtley, D. M. Halat, M. D. McIntyre, B. C. Eigenbrodt, R. A. Walker, *Anal. Chem.* **2012**, *84*, 9745–9753; b) E. Brightman, R. Maher, G. J. Offer, V. Duboviks, C. Heck, L. F. Cohen, N. P. Brandon, *Rev. Scientific Instr.* **2012**, *83*, 053707; c) S. Deabate, G. Gebel, P. Huguet, A. Morin, G. Pourcelly, *Energy Environ. Sci.* **2012**, *5*, 8824–8847.
- [8] a) K.-C. Chang, B. Ingram, B. Kavaipatti, B. Yildiz, D. Hennessy, P. Salvador, N. Leyarovska, H. You in *Materials Research Society Fall 2008 Meeting*, Vol. 1126, **2008**; b) B. Yildiz, K.-C. Chang, D. Myers, J. D. Carter, H. You in *7th European Solid Oxide Fuel Cell Forum*, **2006**; c) K.-C. Chang, B. Ingram, P. Salvador, B. Yildiz, H. You in *Materials Research Society Fall 2013 Meeting*, Vol. 1495, **2013**.
- [9] R. J. Woolley, M. P. Ryan, S. J. Skinner, *Fuel Cells* **2013**, *13*, 1080–1087.
- [10] G. Nurk, T. Huthwelker, A. Braun, C. Ludwig, E. Lust, R. P. W. J. Struis, *J. Power Sources* **2013**, *240*, 448–457.
- [11] a) D. E. Starr, Z. Liu, M. Havecker, A. Knop-Gericke, H. Bluhm, *Chem. Soc. Rev.* **2013**, *42*, 5833–5857; b) E. J. Crumlin, E. Mutoro, W. T. Hong, M. D. Biegalski, H. M. Christen, Z. Liu, H. Bluhm, Y. Shao-Horn, *J. Phys. Chem. C* **2013**, *117*, 16087–16094; c) E. J. Crumlin, E. Mutoro, Z. Liu, M. E. Grass, M. D. Biegalski, Y.-L. Lee, D. Morgan, H. M. Christen, H. Bluhm, Y. Shao-Horn, *Energy Environ. Sci.* **2012**, *5*, 6081–6088; d) F. El Gabaly, K. F. McCarty, H. Bluhm, A. H. McDaniel, *Phys. Chem. Chem. Phys.* **2013**, *15*, 8334–8341.
- [12] a) A. V. Shchukarev, D. V. Korolkov, *Centr. Eur. J. Chem.* **2004**, *2*, 347–362; b) R. P. Vasquez, *J. Electron Spectrosc. Relat. Phenom.* **1991**, *56*, 217–240; c) P. A. W. van der Heide, *Surf. Interface Anal.* **2002**, *33*, 414–425.
- [13] a) N. S. McIntyre, M. G. Cook, *Anal. Chem.* **1975**, *47*, 2208–2213; b) L. Dahéron, R. Dedryvère, H. Martinez, M. Ménétrier, C. Denage, C. Delmas, D. Gonbeau, *Chem. Mater.* **2008**, *20*, 583–590.
- [14] a) J. Stoch, J. Gablankowska-Kukucz, *Surf. Interface Anal.* **1991**, *17*, 165–167; b) J.-C. Dupin, D. Gonbeau, P. Vinatier, A. Levasseur, *Phys. Chem. Chem. Phys.* **2000**, *2*, 1319–1324.
- [15] M. Imamura, N. Matsubayashi, H. Shimada, *J. Phys. Chem. B* **2000**, *104*, 7348–7353.

- [16] A. F. Carley, S. Rassias, M. W. Roberts, *Surf. Sci.* **1983**, *135*, 35–51.
- [17] a) W. Jung, H. L. Tuller, *Energy Environ. Sci.* **2012**, *5*, 5370–5378; b) Y. Chen, W. Jung, Z. Cai, J. J. Kim, H. L. Tuller, B. Yildiz, *Energy Environ. Sci.* **2012**, *5*, 7979–7988.
- [18] a) M. E. Lynch, M. Liu, *J. Power Sources* **2010**, *195*, 5155–5166; b) M. E. Lynch, L. Yang, W. Qin, J.-J. Choi, M. Liu, K. Blinn, M. Liu, *Energy Environ. Sci.* **2011**, *4*, 2249–2258.
- [19] B. Ravel, M. Newville, *J. Synchrotron Radiat.* **2005**, *12*, 537–541.

Received: July 11, 2014

Published online on September 9, 2014